Title
Study of High Aspect Ratio NLD Plasma Etching and Postprocessing of Fused Silica and Borosilicate Glass

Journal
Journal of Microelectromechanical Systems, 24(4)

ISSN
1057-7157

Authors
Ahamed, Mohammed J
Senkal, Doruk
Trusov, Alexander A
et al.

Publication Date
2015

DOI
10.1109/jmems.2015.2442596

Study of High Aspect Ratio NLD Plasma Etching and Postprocessing of Fused Silica and Borosilicate Glass

Mohammed J. Ahamed, *Member, IEEE*, Doruk Senkal, *Student Member, IEEE*, Alexander A. Trusov, *Member, IEEE*, and Andrei M. Shkel, *Fellow, IEEE*

***Abstract*— In this paper, we report magnetic neutral loop discharge (NLD) plasma etching of fused silica (FS) and borosilicate glass (BSG), demonstrating high aspect ratio deep etch (100 μm) with vertical walls (<3° deviation from vertical). This paper for the first time presents the systematic study of FS and BSG deep etching in NLD plasma. Four different masking materials have been explored including metal, amorphous silicon, bonded silicon, and photoresist. Etch parameters were optimized to eliminate unwanted artifacts, such as micro-masking, trenching, and faceting, while retaining a high aspect ratio (up to 7:1 for FS and 8:1 for BSG). In addition, a method for sidewall roughness mitigation based on postfabrication annealing was developed, showing the sidewall roughness reduction from the average roughness (R_a) 900 to 85 nm. Further advances in deep plasma etching processes may enable the use of FS and BSG in the fabrication of precision inertial MEMS, micro-fluidic, and micro-optical devices. [2015-0078]**

***Index Terms*— Microfabrication, plasma etching, fused quartz, fused silica, glass etching, roughness reduction.**

I. Introduction

FUSED SILICA is the desired material for MEMS and micro-optical devices for its outstanding temperature stability, high electrical resistance, low optical loss, and low internal thermo-elastic loss [1]. Borosilicate glass is also preferred in many biochemical and micro-fluidic applications due to its low cost, chemical resistance, thermal insulation, anodic bonding capability, and optical transparency [2]. Despite the potential advantages of Fused Silica (FS) and Borosilicate Glass (BSG), the chemical inertness of SiO_2 prevents fabrication of smooth, high-aspect ratio structures using conventional fabrication techniques.

Wet chemical and dry plasma etchings are the two main wafer-level fabrication processes for both FS and BSG. Wet etching using HF (Hydrofluoric acid) demonstrated deep glass etching with smooth sidewalls. However, due to its isotropic etching the aspect ratio is limited [2]. In contrast, anisotropic dry plasma etching can enable high aspect ratio etching. However compared to silicon, the glass dry etching suffers from orders of magnitude lower aspect ratio, limited mask selectivity, slower etch rate, and high surface roughness [3].

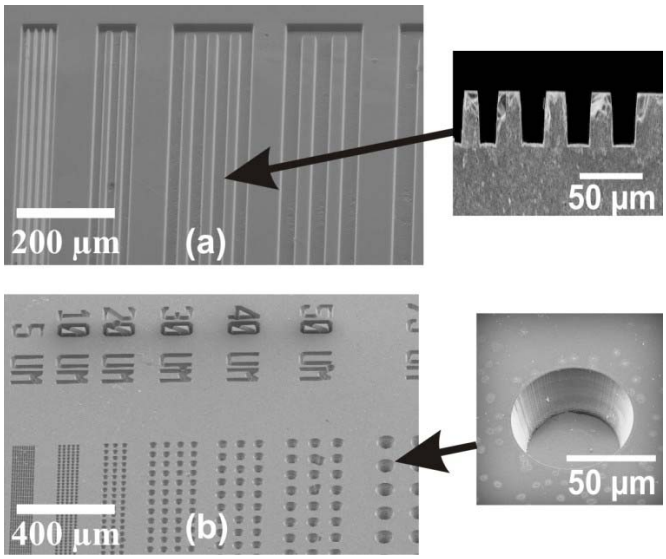

Fig. 1. SEM images showing deep NLD plasma etched microfeatures on (a) Fused Silica and (b) Borosilicate glass.

To address the challenges of deep dry etching of FS and BSG, different plasma sources (ICP, RIE, RF, Microwave) and various masking materials were explored [4]–[16]. For example, fused silica etching to a depth of 55 μm with 86° vertical wall etching was demonstrated using a SU-8 photoresist mask in Reactive Ion Etching (RIE) plasma [16]. Etch depth of about 100 μm and aspect ratio of 3:1 were demonstrated on fused silica using a silicon mask in RIE plasma [8]. Using Nickel (Ni) mask, aspect ratios of 2 to 4 were demonstrated in [4] and [8]. Metal masks showed promise with high mask selectivity and deep etching, but were susceptible to micro-masking [4], [8]. KMPR photoresist mask was used for deep etching and about 2:1 selectivity was demonstrated in [12] and [15]. Despite these efforts, challenges of mask selectivity, higher aspect ratio, and etch quality in deep etching of glass do remain.

Manuscript received March 17, 2015; accepted June 3, 2015. Date of publication June 23, 2015; date of current version July 29, 2015. This work was supported by the Defense Advanced Research Projects Agency under Grant W31P4Q-11-1-0006. Subject Editor H. Seidel.

The authors are with the MicroSystems Laboratory, University of California at Irvine, Irvine, CA 92697 USA (e-mail: jahamed@gmail.com; dsenkal@uci.edu; atrusov@uci.edu; ashkel@uci.edu).

Color versions of one or more of the figures in this paper are available online at http://ieeexplore.ieee.org.

Digital Object Identifier 10.1109/JMEMS.2015.2442596

In contrast to classical ICP and RIE systems, in this work we studied Magnetic Neutral Loop Discharge (NLD) plasma (ULVAC NLD 570) system for FS and BSG etching. NLD plasma is known for generating high density and uniform plasma at low pressures and temperatures [17], [18]. It helped to achieve a high level of directionality and etch rate, that are required for SiO_2 etching. In the NLD plasma apparatus, an external Radio Frequency (RF) electric field was used to create plasma along a neutral magnetic field [18]. The coupling between the RF and magnetic field assured the ion directionality, achieving a high flux of ion bombardment. Our hypothesis was that such high density plasma would provide a platform for deep etching of FS and BSG. It would also provide a uniform ion-bombardment that would allow to overcome the challenges in deep etching of FS and BSG.

We studied the NLD plasma etching with three new approaches to achieve high aspect ratio features: (1) mask selection for NLD based deep etching, (2) optimum NLD plasma conditions to obtain defect-free etching, and (3) post-processing step to mitigate sidewall roughness. Four masking materials: electroplated Ni, KMPR photoresist, bonded silicon, and deposited amorphous silicon were explored. Etch parameters, such as etching/inert gas, antenna power, bias power, chamber pressure, and chamber temperature were optimized. Results were compared in terms of etch depth, sidewall roughness, sidewall angle, and etch defects. Finally, the optimized process was applied for fabrication of micro-features out of both FS and BSG, as shown in Figure 1.

In the following section we will present various etch masks and their selectivities. Section III presents the effect of plasma parameters on aspect ratio of etching. In section IV, we will present a post-processing method for mitigation of sidewall roughness. The paper concludes with an example of how the optimized etch process can be used for fabrication of MEMS micro-wineglass resonators.

II. Variation of Etch Mask

We explored four etch masks in the NLD system: metal (Ni), bonded silicon, photoresist (KMPR), and deposited amorphous silicon (a-Si) [19]. For these masking materials, the plasma parameters were varied as follows: etching gas C_3F_8 with the flow from 10 to 40 sccm (standard cubic centimeter per minute), dilution gas Argon (Ar) with the flow varied from 0 to 200 sccm, bias power from 50 to 200 W, antenna power from 800 to 1600 W, and chamber pressure from 5 to 15 mT. We tested etching parameters for both FS and BSG. In this section, we present the results for each masking material.

A. Electroplated Nickel Mask

A low-stress 5 μm thickness electroplated Nickel (Ni) metal mask was developed for both FS and BSG. The mask was able to resolve a minimum feature size of 2 μm. Chromium (Cr) and gold (Au) was used as a seed layer for electroplating. After the electroplating step, the unwanted seed layer was removed by wet etching using Cr and Au etchants, respectively. The selection of Cr and Au allowed to prevent the chemical etching of the Ni mask. The choice of seed material, masking material, and etching chemistry helped to resolve very fine features, on the order of a couple of microns.

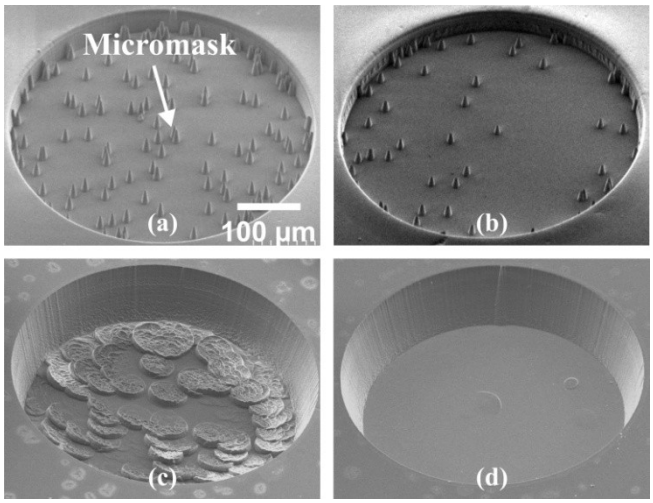

Fig. 2. Mitigation of micro-masking by process optimization. (a)-(d) Ar flow varied from 10 to 90 sccm and power from 80 to 150 W with 30 sccm flow of C_3F_8.

The mask was then utilized to etch both FS and BSG using the NLD plasma system. In our study we discovered that the challenge of using metal mask in the dry etching is the significant re-depositing of masking material into the etched area of substrate during etching. These re-deposited masking materials created unwanted pillar-like features on the substrate (Figure 2a), known as micro-masking.

Micro-masking reduces the aspect ratio, feature accuracy, etch rate, thus limiting the maximum achievable etch depth. We found that some of the pillars, created from micro-masking, varied in sizes between 1 and 2 μm in diameter, at the earlier stage of etching (10 μm deep). These micro-masks were increased to 10-15 μm when etched deeper, on the order of 100 μm. It is necessary to eliminate the micro-masking to preserve the feature resolution. We found that it would ultimately reduce the device performance. For example, these defects would affect the frequency symmetry and degrade the capacitive transduction efficiency of a MEMS device when implemented as a resonant structure, such as a gyro or a clock.

Reduction of micro-masking has been a key challenge in glass etching. Our results showed that iterating only one etching parameter was insufficient for reduction of micro-masking. For example, higher amounts ($>$120 sccm) of dilution gas (e.g., Ar) increased the ion milling, thus reducing the quality of features. Higher amount of etching gas ($>$30 sccm) increased the coarse etching, reduced selectivity, and increased micro-masking. In the NLD system, a 1:3 ratio of etching gas to dilution gas flow gave the best value for reduction of micro-masking (Figure 2d). In addition, a higher bias power also increased the ion milling, that consequently reduced the micro-masking. Higher bias power ($\sim$200W) reduced micro-masking, but created defects due to higher ion milling. Our results showed that a bias power (120 W) to antenna power (1600 W) produced the best defect-free etching (Figure 2).

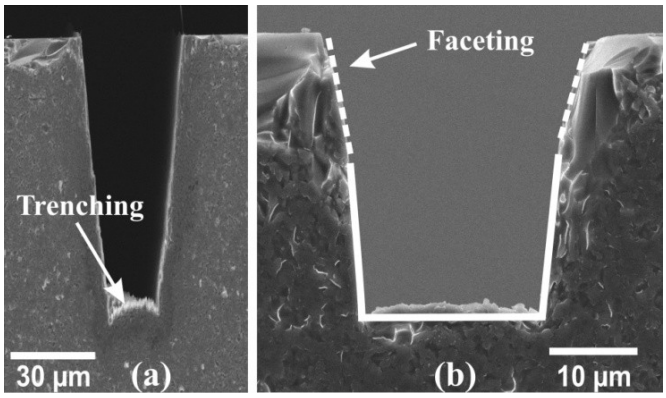

Fig. 3. Formation of (a) trenching at the bottom surface on FS as a result of high content of dilution gas (Ar), (b) faceting of FS due to a-Si mask.

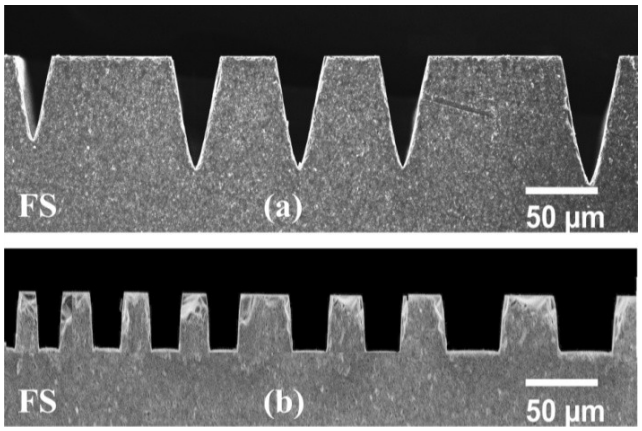

Fig. 4. Illustration of aspect ratio dependent etching, (a) the feature size dependent issue was mitigated as shown in figure (b) we used a process receipe of C_3F_8 at 20 sccm, Ar at 20 sccm, antenna power at 1200 W, bias power at 120 W, and a-Si etch mask.

We found that chamber contamination with Ni residue also contributed to an increase in the micro-masking. To minimize the chamber contamination from the etching residue, an alternate etching and oxygen plasma cleaning (90 sccm O_2, 1500 W antenna, and 50 W bias) were used. Each etching step was followed by a cleaning step. Finally, a minimal to no micro-masking was achieved using the flows of C_3F_8 at 30 sccm, Ar at 90 sccm, antenna power at 1600 W, bias power at 120 W, and pressure of APC at 3mT with Trigger at 15 mT (Figure 2d). With the optimized process, deeper (70 to 100 μm) etching was achieved even with the smaller openings, on the order of 5 μm.

B. Amorphous Silicon Mask

In this part of our study, a silicon mask was explored for glass etching leveraging the high etch selectivity of materials. We tested low stress amorphous silicon as a masking material.

The amorphous silicon (a-Si) mask was introduced by depositing low stress 3.5 μm silicon on both FS and BSG. The a-Si layer was then etched using the Bosch DRIE (STS Multiplex) process. In the magnetic NLD plasma, the non-metallic a-Si mask showed a higher etch rate of 0.65 μm/min for BSG and 0.75 μm/min for FS. The etching recipe was different from the Ni mask described previously. The higher amount of Argon (Ar) was no longer required because the micro-masking was eliminated. However, faceting and trenching were noticed with the a-Si mask (Figure 3). To minimize these defects we investigated different plasma conditions. In NLD plasma, etching with a-Si mask showed that a higher amount of antenna power was not required. An increase in the flow of the etching gas to above 20 sccm did not produce higher etch rate. Results showed that with C_3F_8 at 20 sccm, Ar at 20 sccm, antenna power at 1200 W, bias power of 120 W, and chamber pressure of 3 mT produced the optimum etching results. It showed a mask selectivity of 8:1. With 8:1 selectivity, a-Si mask was not favorable for 100 μm deep etching because a 12 μm or thicker mask would be needed. However, the maximum practical amount of a-Si deposition was limited by several microns. We found that a thicker layer of a-Si had adhesion issues showing mask delamination and multiple defects present when etched for longer time.

Our results with a-Si mask in NLD plasma showed that the etch depth was independent of the mask opening. This means the aspect ratio dependent etching was low, when mask opening varied from 10 μm to 500 μm (Figure 4b). The sidewall angle in etched features was also investigated. When the sidewall angle was appeared to be tapered we observed that the trenches would close, preventing the plasma from etching any further deeper (Figure 4a). This would prevent achieving higher aspect ratio etching. To improve this we iterated masking material. Nearly vertical sidewall was achieved using a-Si mask with 1:1 ratio of etching gas to dilution gas, as shown in Figure 4b.

C. Bonded Silicon Mask

In the previous section, we concluded that utilization of a-Si mask is limited by its lower mask thickness. One way to overcome this limitation is to use a thicker, bonded silicon, mask. A thicker silicon layer can be bonded to glass using, for example, the anodic bonding technique. In this study, a bonded silicon mask was achieved by using plasma assisted fusion bonding between silicon and FS or anodic bonding between silicon and BSG. High strength plasma bonding, which was earlier reported in [1], was used for the bonding. The bonded silicon mask was patterned using the Bosch DRIE (STS Multiplex) process. It was then used as a mask in the NLD plasma for etching both FS and BSG. The bonded silicon mask was thicker, and as predicted, the thicker mask layer prevented reactive ions penetrating into deeper tranches of smaller openings. Therefore, as a result of high mask thickness, deep etching was not possible for smaller mask openings ($<$20 μm). The phenomena limited the fabrication of small capacitive gaps, making it not suitable for the dynamics MEMS with capacitive detection, as larger capacitive gaps would reduce the transduction efficiency of the device.

To overcome the aspect ratio dependent etching with the bonded silicon mask, we varied Ar from 30 to 120 sccm and antenna power from 800 to 1600 W. During our experiments

TABLE I
COMPARATIVE ANALYSIS OF DIFFERENT ETCH MASKS

	Metal (Ni)	KMPR	Bulk Silicon	Amorphous Silicon
Selectivity	70:1	0.7:1	30:1	8:1
Etch rate BSG(μm/min)	0.35	0.20	0.60	0.65
Etch rate FS (μm/min)	0.45	0.30	0.50	0.75
Wall angle (θ)	84^0	82^0	87^0	86^0
Cost	Low	Very low	High	High
Depth of etching	Deep (>100μm)	Medium	Medium	Shallow (~30μm)
Aspect ratio dependence	High	Moderate	Moderate	Very Low
Key process parameter C_3F_8 (sccm) + Ar (sccm)	30, 90	20,10	20, 20	20, 20

with the Ar flow and antenna power, the bias power was kept constant. This was done because an increase in the bias would increase the ion bombardment. Increasing the gas flows or antenna power would improve the aspect ratio of etching. However, we also noticed that an increase in the flow rate of the dilution gas Ar to above 75 sccm, or an increase in antenna power to above 1200W, would increase defects. This is because an increase in the rate of Ar and antenna power may increase the rate of ionization of the etching gas, that would create defects. With bonded silicon mask, the optimum Ar flow rate was found to be 50 sccm and antenna power 1200W. Any increase in these parameters did not improve the aspect ratio.

The precision deep etching of small features (<20 μm) was a challenge with the bonded silicon mask. The other challenges of bonded-silicon mask were the cost and fabrication complexity associated with wafer bonding. The thick silicon layer bonded to a glass often caused the wafer to bow during etching due to material mismatch in thermal expansion. To avoid heating and wafer bowing, etching and cooling steps were alternated. Etching for five minutes and cooling for five minutes helped to avoid the wafer bow, delamination, or breakage. The advantage of bonded silicon mask was its 30:1 selectivity (Table I). The other advantage that we noticed while using it in the NLD plasma, was that there was no mask re-deposition (micro-masking). The etched residue was lower, which allowed the fabrication of precision features with low roughness.

D. KMPR Photoresist Mask

Photoresist masks are cheaper and simpler to fabricate compared to metal or silicon masks. KMPR 1025 (Microchem Corp) was used in ICP/RIE based etchers for etching glass or fused silica [12], [15]. KMPR was selected in this study because it is non-metallic, simple to fabricate, and easy to remove after the etching process. The KMPR photoresist mask was processed using the standard lithography techniques. Our results showed limited selectivity (<1) of KMPR to glass, making it not a suitable masking material for a deeper etching (Table I). The other disadvantage noticed in our experiment was the re-deposition of large amount of consumed KMPR on the chamber, sidewalls, and substrate. For the KMPR mask, we found that a higher amount of Ar was not optimal, as it decreased the selectivity. Due to a large photoresist contamination, an alternating of etching and O_2 plasma cleaning were necessary to reduce the contamination. A chamber cleaning for 15 minutes was performed after each etching steps for 15 minutes. The best etching recipe for KMPR was composed of C_3F_8 of 20 sccm, Ar 10 sccm, antenna power at 1200 W, and bias at 80 W.

In this section we discussed four different masking materials for NLD plasma etching of FS and BSG. Our results are summarized in Table-I. The comparison shows that for achieving both higher selectivity and deeper (100 μm) etching, a Ni metal mask showed the best overall result.

E. Conclusion of Mask Selection

Amorphous silicon mask showed an aspect ratio independent etching, 8:1 selectivity, more vertical wall angle, low defect, and less roughness. Therefore, a-Si mask was concluded to be suitable for up to a limited depth etching, for example micro-fluidic features. The KMPR resist was cost effective and suitable for shallow etching. Bonded silicon mask required a complicated bonding and involved yield issues related to bonding, however it showed no mask re-deposition issues. For our deep etching application, which was the capacitive resonant MEMS, we selected Ni metal mask appreciating its high selectivity when etching deep features.

III. VARIATION OF PLASMA CONDITIONS

Aside from masking material, the other important parameters in NLD plasma glass etching are factors such as plasma power, gas flow, and substrate temperature. In this section, we present the characterization of the above mentioned plasma parameters, with the goal of finding optimal parameters for FS and BSG etching.

A. Plasma Power

The plasma power relates to plasma density and ion energy, and is dependent on antenna power and bias power in the system [18]. The etch rates as a function of plasma powers are shown in Figure 5. Our results showed that when the antenna power was increased, the etch rate was proportionally increased for both FS and BSG, as shown in Figure 5. However, increasing the bias power comes with a cost. At higher bias power, our results showed that the ion bombardment increased, creating undesirable defects and roughness on the sidewalls of features.

Previous study with similar NLD plasma for surface processing [18] showed that the increase in antenna power increased the ion density. The higher antenna power created higher plasma density and ion concentration, which helped to increase the etch rate. Our experiments showed that for Ni mask a higher antenna power (e.g., 1400 to 1600W) can be safely used for achieving higher etch rate (e.g., 0.3 to 0.5 μm/min) without significantly reducing mask selectivity.

B. Gas Flow

The amount of etching gas flow plays an important role in the dry etching process [8], [18], [20]. We applied the

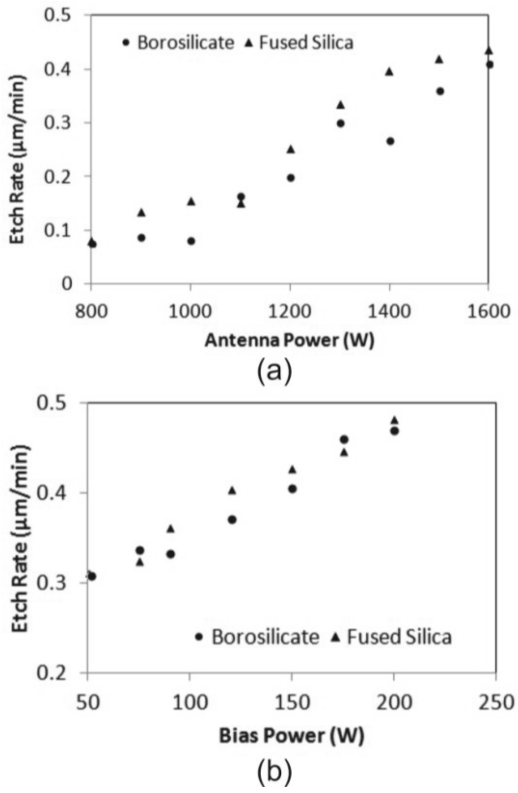

Fig. 5. Etch rate of glass vs. antenna power and bias power with 30 sccm C_3F_8, 90 sccm Ar. Bias power was kept at 80W when antenna power was changed in (a). Similarly, antenna power was at 1400W when bias power was varied in (b).

methodology to the NLD plasma etching of FS and BSG. In our experiments, C_3F_8 and Ar gas chemistry were used. The plasma etching is achieved by the reactive species created in result of the dissociation of fluorinated C_3F_8 etching gas. The etching process is completed by two simultaneous steps, these are: (1) chemical reactions of the etching gas with the glass surface and (2) physical etching due to ion bombardment [14]. The bombardment of ions contributes to an anisotropic and directional etch. In the NLD system, the electric field inside the chamber directs ions vertically [18]. In our experiments, the flow of etching gas C_3F_8 was varied from 10 to 40 sccm and the dilution gas Ar varied from 0 to 200 sccm. Increasing the flow of etching gas C_3F_8 increased the etch rate only by up to 30 sccm (Figure 6), any further increase would reduce the effective etch rate. It also reduced the mask selectivity and increased defects, for both FS and BSG. Increased amounts of etching gas in the chamber created higher amount of by-products. As a result, the etch by-products re-deposited and slowed down the etch rate as well as increased feature roughness on sidewalls.

The effect on etching of addition of Ar to the gas chemistry has been debated in literature [7], [18], [20]. Adding higher amount of Ar in an ICP system would decrease the etch rate [7]. In [18], it was shown that SiO_2 etching was increased by adding Ar for up to a certain value. However, including Ar to the gas chemistry may increase the physical etching due to ion bombardment and may contribute to increase in the sidewall angle [13]. In our experiment with the

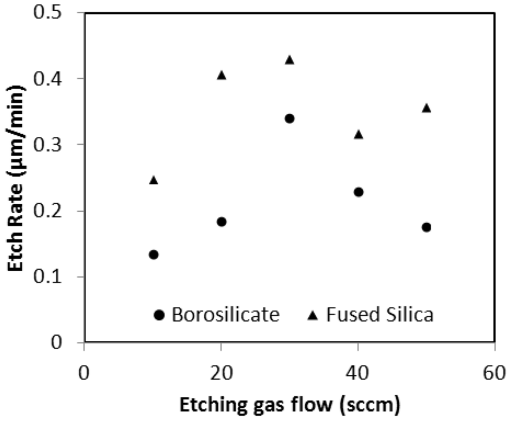

Fig. 6. Etch rate vs ethching gas flow rate.

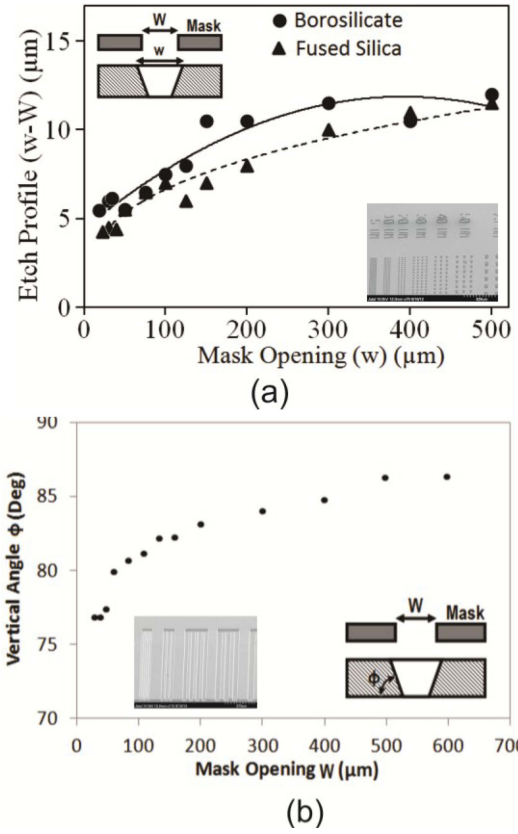

Fig. 7. Etch profile (a) and wall angle (b) with mask opening.

NLD plasma, we found that 10 to 50 sccm of Ar helped in reducing contamination on the etched surface because of the ion bombardment. However, the higher amount of Ar (>120sccm) increased non-uniformity of etching and produced defects on micro-structures.

C. Mask Opening

Mask opening to depth of etching (aspect ratio) is an important parameter that can determine the design flexibility and etch capability of the process. Therefore, we investigated it for both FS and BSG. Etching depth, sidewall angle, and etch profile with mask opening are plotted in Figure 7. The aspect

ratio dependence on the etch rate was higher when using Ni mask. The etch depth was higher at larger mask openings (>300 μm) and lower at smaller mask openings (<50 μm). This effect can be explained by two reasons: (1) the full plasma power does not propagate inside the small openings and (2) the buildup of residues on the sidewall narrows the etch opening. This former effect was negligible when a thinner etch mask was used (e.g., amorphous silicon mask).

D. Substrate Temperature

Substrate temperature has a role in etch rate, mask selectivity, and etch quality. In addition, if the substrate temperate is too high, some masking materials may not survive (i.e., photoresist). It may contribute to lower mask selectivity. Usually, in the NLD plasma system the substrate temperature is controlled by the coolant circulator. In our experiments, it was varied from −20 °C to +20 °C. By increasing the coolant temperature the substrate temperature was increased, which in turn increased the etch rate. For example, the etch rate was increased from 0.31 μm/min to 0.59 μm/min, when the coolant temperature was increased from −20 °C to +10 °C. However, we noticed that at higher temperatures the masking material re-deposition rate increased, creating micro-masking. Our result showed that for deeper etching a lower substrate temperature (e.g., coolant set temperature at −10 °C) was desirable.

E. Etching Time

Due to chemical inertness of material, FS and BSG etch rate are usually slower as compared to Si etching, taking it longer time to etch deep. One important parameter is finding a suitable maximum allowable etch cycle for continuous etch time. To systematically characterize the phenomena, we varied the etch time from 5 to 53 minutes. We found that longer etching (∼30 min), for both FS and BSG, would reduce the cumulative etch rate. Our results showed that with longer etch time the depth of etching increased for both FS and BSG, but the cumulative etch rate decreased (Figure 8). When the etch time increased to 53 minutes, the accumulation of etch by-products, back sputtering, and re-deposition of etch by-products reduced the etch rate by 30 %, compared to the etch rate achieved after the first 20 minutes. With the photoresist mask, the result was a more significant reduction (∼50 %) in the etch rate. We found that the higher amount of photoresist by-products should be cleaned before performing longer etching. Our results showed that alternating etching and cleaning steps was required for high quality deep etching. Using the NLD plasma etching system, a shorter etching time (∼20mins) was effective for achieving a higher etch rate for deeper etching.

F. Glass Composition and Wall Angle

Different glasses exhibited slightly different etching results. FS and BSG have different silica matrix, which would result in different etch behavior. NLD etching characteristics of both FS and BSG were compared in this study. BSG etched faster for the first 20 to 30 μm of deep etching because of the release

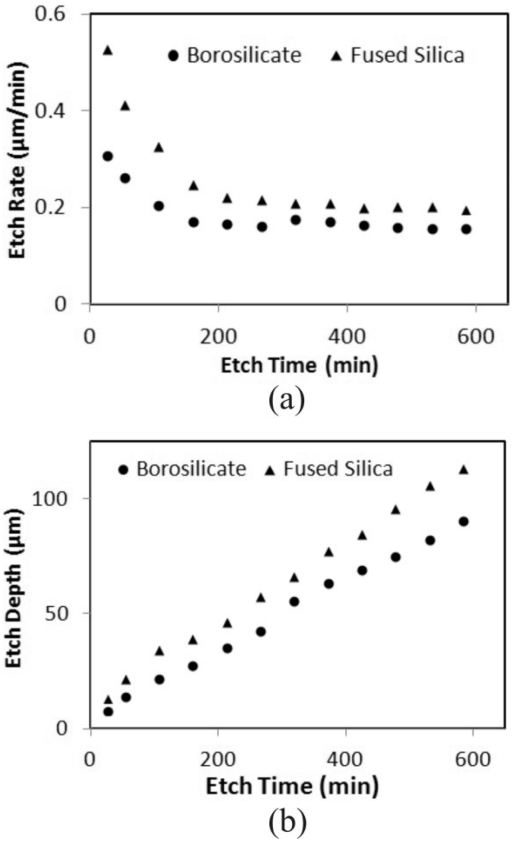

Fig. 8. (a) Etch rate vs time showing that contineous etching decreases the etch rate for both FS and BSG. FS etches faster compared to BSG. (b) Etch depth vs time shows that depth increases with contineous etching, although etch rate decreases.

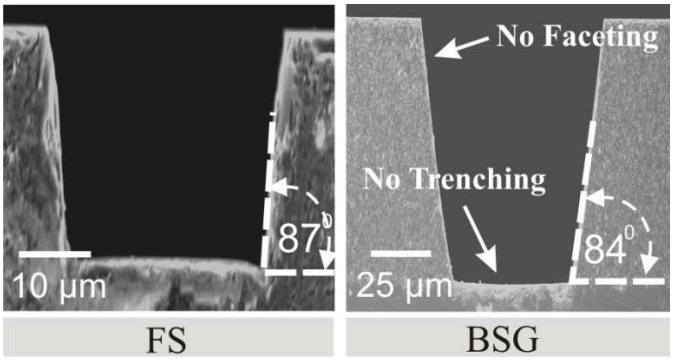

Fig. 9. Deep etching of FS with vertical wall angle of 87° and deep etching of BSG with vertical wall angle of 84°. Deep etching of 100 μm with no faceting or trenching was achieved (right).

of impurities. For deeper etching (∼100 μm), the overall etch rate of FS was higher compared to BSG.

After deep etching, nearly vertical sidewall etching was possible on FS (87°) and on BSG it was about 84°, as shown in Figure 9. Results showed that etching gas C_3F_8 flow of 30 sccm and dilution gas Ar flow of 90 sccm resulted in a balanced chemical and physical etching, creating a nearly vertical wall etching. In addition, the lower pressure of 3 mT, as well as the coupling between the 1500 W antenna power

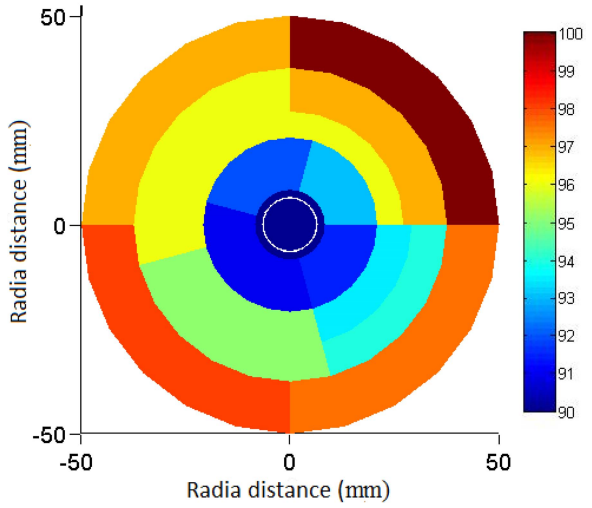

Fig. 10. Etching variation across the wafer showing the maximum of 10% depth variation across the wafer, with more uniform etching at the center and higher etching at the outer perimeter.

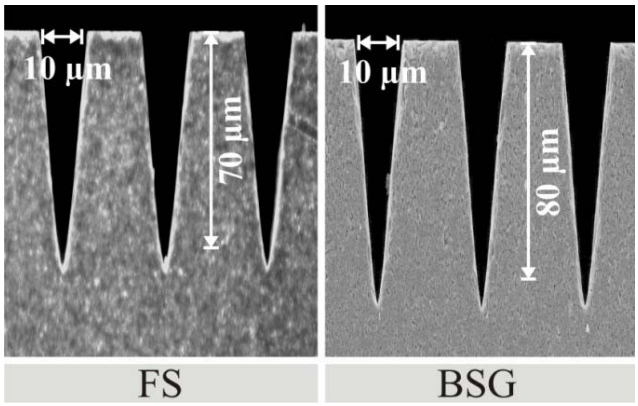

Fig. 11. High aspect ratio deep etching of FS and BSG glass was achieved in a small mask opening of 10 μm.

and 50 W bias powers, contributed to directionality of ion bombardment, creating higher vertical sidewall.

G. Etch Variation Across Wafer

Etch variation across a wafer is an important parameter for designing the wafer-level fabrication process. To quantify the etch variation across the wafer we measured the final etch depth at various radial points across the wafer for the same mask openings. Results are shown on the surface plot in Figure 10. The etch depth measured at the center of the wafer was found to be uniform. However, the depth was less uniform towards the edge of the wafer. The etch rate was higher at the edges compared to etch rate at the center of the wafer.

The average maximum variation in the final etch depth was found to be about 10%. And the maximum aspect ratio obtained across the wafer was 7:1 with FS and 8:1 with BSG, as shown in Figure 11.

H. Roughness

Roughness of etched surfaces was measured for both FS and BSG using an atomic force microscope (AFM) from

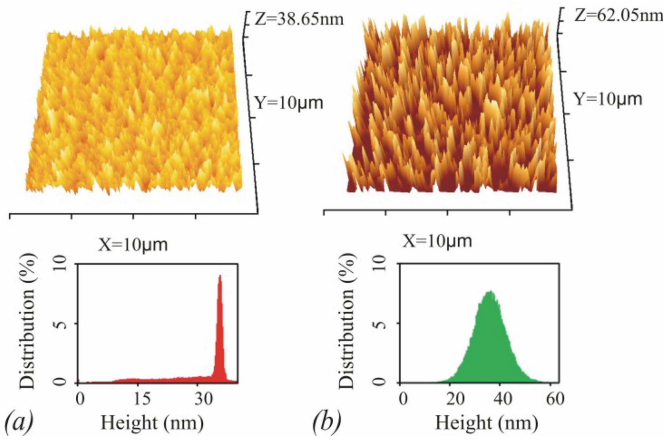

Fig. 12. AFM surface morphologies of (a) FS and (b) BSG after 10 μm deep etching show BSG surface roughness has sharper peaks due to release of impurities from SiO_2 matrix, as compared to FS.

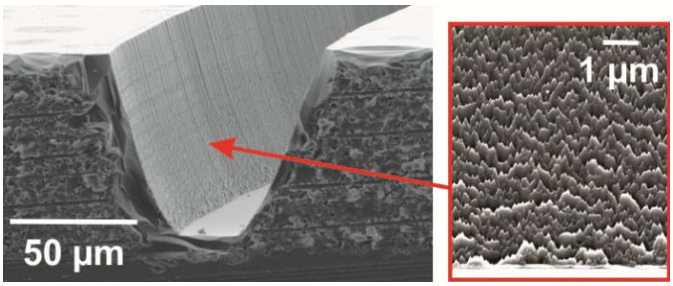

Fig. 13. Highly rough un-treated vertical-wall surface after 100 μm deep glass etching.

Pacific Nanotechnology (Nano-R). After etching 10 μm deep, BSG showed a rough surface morphology compared to FS (Figure 12). The roughness was increased with the duration of etching. The presence of volatile impurities in the SiO_2 matrix is likely associated with a relatively rough surface of BSG. In the next section, we present a post-processing method for roughness reduction.

IV. Post Processing: Sidewall Roughness Reduction

Despite the careful optimization of etch parameters, a certain degree of plasma damage and associated sidewall roughness are unavoidable in any dry etch process. For example, after 100 μm deep etching, the average roughness of the sidewall surfaces was found to be about 900 nm R_a, as shown in Figure 13. It was caused by ion-bombardment and excessive residue deposition.

High sidewall roughness is unwanted because it can affect the symmetry of the structural element [21] or create an unwanted dissipation in the resonant MEMS [22]. Such rough sidewalls are not desirable for the MEMS wineglass resonators, for example, the structures that motivated this study. In the wineglass resonator, the majority of vibratory energy is located at the perimeter of the device, where the dry etched sidewalls are located. The surface roughness are also undesirable in other microsystems devices, such as in

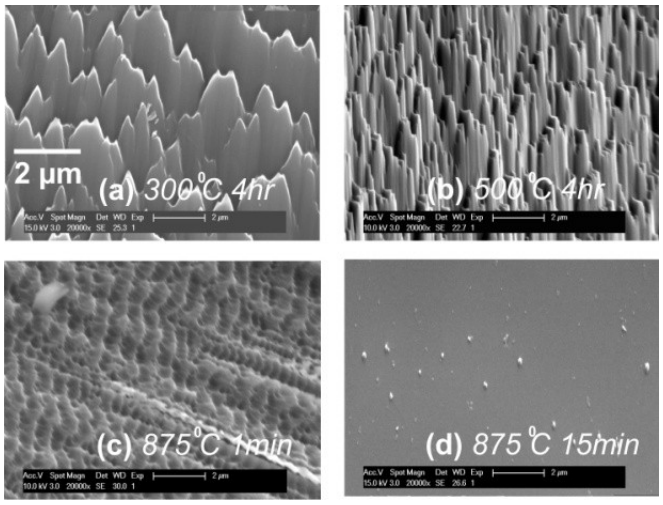

Fig. 14. SEM surface morphologies of BSG showing roughness decrease with increase in temperature and duration of post-etch annealing, producing smooth surfaces, from (a) to (d).

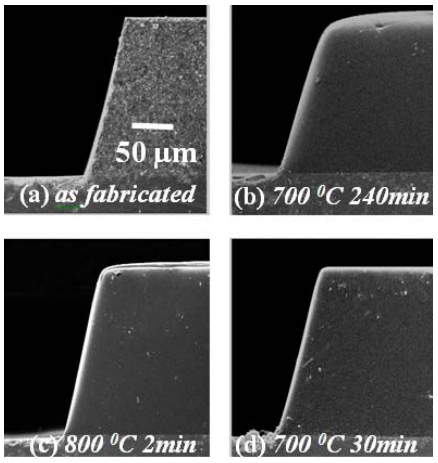

Fig. 15. The treatment temperature and duration time were optimized to improve roughness, while minimizing feature deformation. (a)–(d) Deformation of the edge of the etched feature at different treatment time and temperature.

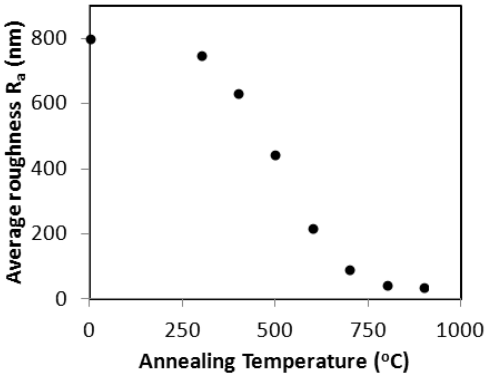

Fig. 16. Average roughness vs annealing temperature shows that roughness decreases significantly, at near the softening temperature of glass (e.g., 820 °C for BSG).

micro-fluidic or micro-optical applications. In this section, we explore a post-fabrication method for reducing the sidewall roughness.

To a lesser extent, the sidewall roughness is also an issue in the silicon deep etching process. Researchers have shown that post-etch annealing of silicon can mitigate the issue. For example, smoothing of silicon structures was demonstrated at temperatures exceeding 900 °C [23]. Hydrogen annealing of silicon features on SOI for temperatures over 1100 °C demonstrated roughness improvement from 20 nm to 0.26 nm [24]. Annealing of 3-hexylthiphene polymer, showed roughness increase for temperature 110 °C and then showed a decrease from 0.91 nm to 0.75 nm at 150 °C [25]. Sputtered chromium oxide annealed at 400 °C, demonstrating roughness improvement from 5.5 nm to 3.6 nm [26]. Similar treatment of glass dry etched micro-features has not been investigated.

This study focuses on post-fabrication roughness reduction in glass. We used a post-fabrication thermal annealing method to improve the roughness [27]. Post-fabrication thermal treatment can improve the roughness, producing highly smooth surfaces. However, the thermal treatment may deform the dry etched features. In this study, we evaluated the trade-off space between roughness reduction and shape distortion in order to identify an optimal thermal annealing condition.

Experiments were performed on dry etched (100 μm deep) micro-features sized from 5 μm to 500 μm, for different post-annealing conditions. Two important parameters in the thermal annealing process are temperature and duration. In our study, treatment temperatures varied between 300 °C and 900 °C, with durations between 2 and 240 minutes. Roughness, surface morphologies, and feature deformations were investigated by AFM and SEM. Our results showed that with the increase of treatment time and temperature the surface roughness decreased by orders of magnitude, as seen in Figure 14.

At lower temperature (300 °C), the improvement was small (Figure 14a), and when the temperature was increased to 500 °C the roughness started noticeably improving (Figure 14b). Our explanation is that the roughness is improved because with increase in temperature the glass softens and reflows. At higher temperatures glass softens and its viscosity decreases, consequently the higher reflow would recover the surface smoothness. Figure 16 shows an average roughness improvement with annealing time. Near the softening point of glass the improvement was significant as compared to initial roughness. At the glass transition point, the material reflow was high and it completely recovered the roughness with surface tension force.

However, the trade off in this reflow method was a deformation of features. There was some shape deformation noticed because of reflow of glass, as the deformation varies with temperature and time (Figure 15). We found that when the duration was long the feature deformation was high, creating round edges (Figure 15b), but the roughness improved significantly with the duration of treatment (Figure 17). Similarly, when the temperature was high (e.g., 900 °C), the deformation was high and roughness improvement was significant. Also, at higher temperature, the longer duration time was not required because the glass was at the transition temperature, resulting in low viscosity and high reflow. For example,

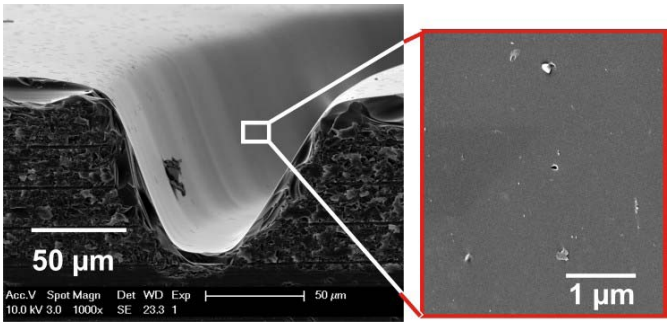

Fig. 17. SEM view of thermally treated wall surface (700 °C, 4 hrs), dramatically improving the roughness creating smooth wall surface (inset).

TABLE II
COMPARATIVE ANALYSIS OF DIFFERENT ANNEALING PROCESS PARAMETERS

Treatment Temperature (^{0}C)	Treatment Duration (Min)	Roughness Improvement	Feature Distortion
400	60,240	Low	No
500	60,240	Low	Very low
600	30,240	Moderate	Low
700	30	High	Low
700	240	Very high	Moderate
800	2	Moderate	Low
800	15	High	High
900	2	Moderate	Moderate
900	15	Very high	Very high

Dry Etching Process Parameters
Etch mask- 5 µm Ni, Mask Selectivity 1:70, Etching gas: C_3F_8 30 sccm and Ar 90 sccm, Mask opening from 10 µm to 500 µm, Max etch depth 100 µm, Max Aspect ratio 1:8.

at 875 °C for 1 minute the average roughness (R_a) was reduced from about 1 μm to 110 nm (Figure 14c). We found that to minimize the shape deformation and maximize the roughness improvement an annealing temperature below its transition temperature was optimum. And a higher duration time should be avoided to minimize the deformation.

We derived an optimum treatment regime at 700 °C for 30 minutes, when the roughness (R_a) improvement was 10-times and deformation remained to be low, at <10% (Figure 14d). The average roughness (R_a) decreased from about 900 nm to 85 nm. Table II summarizes the roughness improvement results with the variation of temperature and treatment duration.

V. EXAMPLE

In this section, we outline an application of the optimized etch process for fabrication of micro-wineglass resonators. This application was the initial motivation for the process development presented in this paper.

The deep etching process discussed in the previous sections was successfully applied for the fabrication of 3-D micro-wineglass MEMS resonators, with the NLD plasma etched glass co-fabricating in-situ electrodes (Figure 18a-18b). The overall fabrication process, as shown in Figure 18a, began by

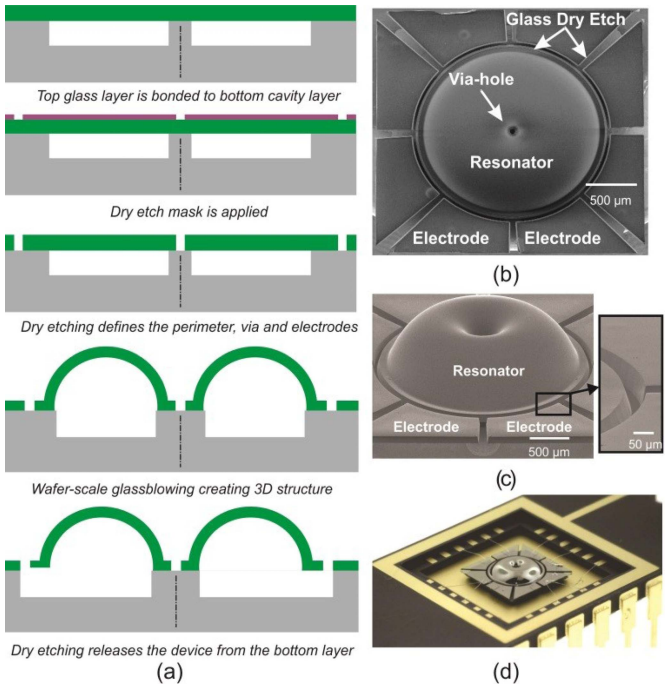

Fig. 18. (a) Basic fabrication flow showing dry etching and micro-glassblowing of wineglass resonator, (b) SEM image showing top down view of the circular resonator perimeter and 100 μm deep glass dry etching creating co-fabricated 8 electrodes, (c) micro-glassblown device with electrodes, and (d) picture of a wire-bonded and packaged device.

defining cavities at the bottom layer and capping the bottom layer with the top glass wafer, defining the device layer. The glass device layer was 100 μm thick and it was dry etched using the process parameters discussed earlier. An electro-plated Ni mask of 5 μm thickness was used as a masking layer. Capacitive gaps and through-hole-via at the center of the device were etched to 100 μm depth for electrostatic transduction. The NLD plasma conditions were set to etching gas (C_3F_8) flow of 30 sccm, dilution gas (Ar) flow of 90 sccm, antenna power of 1600 W, and bias power of 120 W. Electrodes, via hole, and the perimeter of the wineglass structure were fabricated by deep glass etching of the device layer. The fabricated dry etched device structure is shown in Figure 18b. The structure was then micro-glassblown [1] and released by etching the silicon underneath the glass layer [28]. Etching of the silicon substrate resulted in a free-standing wineglass structure and discrete electrodes (Figure 18c). Fabricated resonator was wire bonded and packaged as shown in Figure 18d. It was then tested in a vacuum chamber. The details of the testing and performance characteristics were outlined in our earlier work in [28]. The optimum etching and roughness mitigation helped to achieve an extremely high symmetry, demonstrating <10 ppm frequency symmetry resonators as measured using the n = 2 wineglass mode [28].

VI. CONCLUSION

We have presented a detailed study of NLD (Neutral Loop Discharge) plasma etching for fused silica and borosilicate

glass using metal, photoresist, and silicon etch masks. Etch parameters, such as etching/inert gas, antenna/bias powers, chamber pressure and temperature were optimized for each mask material. Etch depths up to 100 μm were obtained, with the highest aspect ratio of 8:1 on borosilicate glass and 7:1 on fused silica. A post-etch annealing process was demonstrated to improve the sidewall roughness. An average roughness (Ra) was reduced from 900 nm to 85 nm. Finally, the optimized process was utilized for fabrication of micro-wineglass resonators with integrated electrodes. Fabricated devices were actuated using the in-situ dry etched electrode structures. Owing to the low roughness, defect-free etch, the frequency symmetry (Δf/f) on the order of < 10 ppm was measured.

High aspect ratio deep plasma etching processes presented in this paper may enable the use of fused silica and borosilicate glass in precision inertial sensors, micro-fluidics, and micro-optical applications.

ACKNOWLEDGMENT

Devices were designed, developed, and tested in UCI MicroSystems Laboratory. The authors would like to thank UCI INRF staff Jake Hes and Mo Kebaili for their help and suggestions in development of the process.

REFERENCES

[1] D. Senkal, M. J. Ahamed, A. A. Trusov, and A. M. Shkel, "High temperature micro-glassblowing process demonstrated on fused quartz and ULE TSG," *Sens. Actuators A, Phys.*, vol. 201, pp. 525–531, Oct. 2013.

[2] J.-Y. Jin, S. Yoo, J.-S. Bae, and Y.-K. Kim, "Deep wet etching of borosilicate glass and fused silica with dehydrated AZ4330 and a Cr/Au mask," *J. Micromech. Microeng.*, vol. 24, no. 1, pp. 015003-1–015003-16, 2014.

[3] S. Franssila, *Introduction to Microfabrication*, 2nd ed. Hoboken, NJ, USA: Wiley, 2010.

[4] L. Ceriotti, K. Weible, N. F. de Rooij, and E. Verpoorte, "Rectangular channels for lab-on-a-chip applications," *Microelectron. Eng.*, vols. 67–68, pp. 865–871, Jun. 2003.

[5] A. Goyal, V. Hood, and S. Tadigadapa, "High speed anisotropic etching of Pyrex for microsystems applications," *J. Non-Crystalline Solids*, vol. 352, nos. 6–7, pp. 657–663, 2006.

[6] H. Ryu, P. K. Kim, and G. Lim, "Advanced glass etching method exhibiting the controllable etch stop using metal etchant," *J. Micromech. Microeng.*, vol. 22, no. 12, pp. 125010-1–125010-5, 2012.

[7] H. C. Jung, W. Lu, S. Wang, L. J. Lee, and X. Hu, "Etching of Pyrex glass substrates by inductively coupled plasma reactive ion etching for micro/nanofluidic devices," *J. Vac. Sci. Technol. B, Microelectron. Nanometer Struct.*, vol. 24, no. 6, pp. 3162–3164, 2006.

[8] K. Kolari, V. Saarela, and S. Franssila, "Deep plasma etching of glass for fluidic devices with different mask materials," *J. Micromech. Microeng.*, vol. 18, no. 6, pp. 064010-1–064010-6, 2008.

[9] K. Kolari, "Deep plasma etching of glass with a silicon shadow mask," *Sens. Actuators A, Phys.*, vol. 141, no. 2, pp. 677–684, 2008.

[10] M. D. Minnick, G. A. Devenyi, and R. N. Kleiman, "Optimum reactive ion etching of x-cut quartz using SF_6 and Ar," *J. Micromech. Microeng.*, vol. 23, no. 11, pp. 117002-1–117002-6, 2013.

[11] T. Akashi and Y. Yoshimura, "Deep reactive ion etching of borosilicate glass using an anodically bonded silicon wafer as an etching mask," *J. Micromech. Microeng.*, vol. 16, no. 5, pp. 1051–1056, 2006.

[12] T. Ray, H. Zhu, and D. R. Meldrum, "Deep reactive ion etching of fused silica using a single-coated soft mask layer for bio-analytical applications," *J. Micromech. Microeng.*, vol. 20, no. 9, pp. 097002-1–097002-9, 2010.

[13] T. Akashi and Y. Yoshimura, "Profile control of a borosilicate-glass groove formed by deep reactive ion etching," *J. Micromech. Microeng.*, vol. 18, no. 10, pp. 105004-1–105004-9, 2008.

[14] D. A. Zeze *et al.*, "Reactive ion etching of quartz and Pyrex for microelectronic applications," *J. Appl. Phys.*, vol. 92, no. 7, pp. 3624–3629, 2002.

[15] Z. Cao *et al.*, "Drie of fused silica," in *Proc. IEEE 26th Int. Conf. Micro Electro Mech. Syst. (MEMS)*, Taipei, Taiwan, Jan. 2013, pp. 361–364.

[16] H. Chen and C. Fu, "An investigation into the characteristics of deep reactive ion etching of quartz using SU-8 as a mask," *J. Micromech. Microeng.*, vol. 18, no. 10, pp. 105001-1–105001-8, 2008.

[17] W. Chen, K. Sugita, Y. Morikawa, S. Yasunami, T. Hayashi, and T. Uchida, "Application of magnetic neutral loop discharge plasma in deep silica etching," *J. Vac. Sci. Technol. A, Vac. Surf. Films*, vol. 19, no. 6, pp. 2936–2940, 2001.

[18] T. Uchida and S. Hamaguchi, "Magnetic neutral loop discharge (NLD) plasmas for surface processing," *J. Phys. D, Appl. Phys.*, vol. 41, no. 8, pp. 083001–083009, 2008.

[19] M. J. Ahamed, D. Senkal, A. A. Trusov, and A. M. Shkel, "Deep NLD plasma etching of fused silica and borosilicate glass," in *Proc. IEEE Sensors Conf.*, Baltimore, MD, USA, Nov. 2013, pp. 1–4.

[20] L. Lallement, C. Gosse, C. Cardinaud, M.-C. Peignon-Fernandez, and A. Rhallabi, "Etching studies of silica glasses in SF_6/Ar inductively coupled plasmas: Implications for microfluidic devices fabrication," *J. Vac. Sci. Technol. A, Vac. Surf. Films*, vol. 28, no. 2, pp. 277–286, 2010.

[21] B. E. Little, J.-P. Laine, and S. T. Chu, "Surface-roughness-induced contradirectional coupling in ring and disk resonators," *Opt. Lett.*, vol. 22, no. 1, pp. 4–6, 1997.

[22] B. Le Foulgoc *et al.*, "Highly decoupled single-crystal silicon resonators: An approach for the intrinsic quality factor," *J. Micromech. Microeng.*, vol. 16, no. 6, pp. S45–S53, 2006.

[23] K. Kolari, T. Vehmas, O. Svensk, P. Törmä, and T. Aalto, "Smoothing of microfabricated silicon features by thermal annealing in reducing or inert atmospheres," *Phys. Scripta*, vol. T141, pp. 014017–014021, 2010.

[24] M.-C. M. Lee and M. C. Wu, "Thermal annealing in hydrogen for 3-D profile transformation on silicon-on-insulator and sidewall roughness reduction," *J. Microelectromech. Syst.*, vol. 15, no. 2, pp. 338–343, Apr. 2006.

[25] G. Li, V. Shrotriya, Y. Yao, and Y. Yang, "Investigation of annealing effects and film thickness dependence of polymer solar cells based on poly(3-hexylthiophene)," *J. Appl. Phys.*, vol. 98, no. 4, pp. 043704-1–043704-5, 2005.

[26] X. Pang *et al.*, "Annealing effects on microstructure and mechanical properties of chromium oxide coatings," *Thin Solid Films*, vol. 516, no. 15, pp. 4685–4689, 2008.

[27] M. J. Ahamed, D. Senkal, and A. M. Shkel, "Improvement of side-wall roughness in deep glass etched MEMS vibratory sensors," in *Proc. IEEE Int. Symp. Inertial Sensors Syst.*, Laguna Beach, CA, USA, Feb. 2014, pp. 1–2.

[28] D. Senkal, M. J. Ahamed, A. A. Trusov, and A. M. Shkel, "Achieving sub-Hz frequency symmetry in micro-glassblown wineglass resonators," *J. Microelectromech. Syst.*, vol. 23, no. 1, pp. 30–38, Feb. 2014.

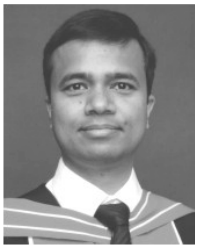

Mohammed J. Ahamed (M'13) received the B.Sc. and M.Sc. (Hons.) degrees in mechanical engineering from the Bangladesh University of Engineering and Technology (BUET), Dhaka, Bangladesh, in 2002 and 2004, respectively, and the M.A.Sc. and Ph.D. degrees in mechanical engineering from the University of Toronto, Canada, in 2006 and 2012, respectively. He was with the MicroSystems Laboratory, University of California Irvine (UCI), USA. He is currently a Postdoctoral Fellow with McGill University, Canada, where his research is focused on developing nanotechnology-based next generation single-cell single-molecule sequencer. During his tenure at UCI, he worked on a Defense Advanced Research Projects Agency funded project for developing precision rate integrating microgyroscope for aerospace applications. He contributed to teaching as a Lecturer with BUET, and a Trainer for teaching assistants with the University of Toronto. He has authored or co-authored dozens of journal and peer-reviewed conference articles. His major research interests include design, fabrication and engineering of microelectromechanical 3-D inertial sensors, gyroscopes, nanotechnology, DNA sequencing, and single-cell and micro/nano-fluidic-based biomedical lab-on-a-chip. He was a recipient of the Canadian Commonwealth and Canadian Connaught Fellowships. He has served as a Reviewer for various journals and conferences. He is a Member of the American Society of Mechanical Engineers and the American Physical Society.

Doruk Senkal (S'13) received the B.S. degree in mechanical engineering from Middle East Technical University, Ankara, Turkey, in 2007, and the M.S. degree in mechanical engineering from Washington State University, Vancouver, in 2009. He is currently pursuing the Ph.D. degree in mechanical engineering with a focus on micro-electromechanical systems (MEMS). He is currently a Graduate Student Research Assistant with the University of California, Irvine Microsystems Laboratory. His research interests include design and control of degenerate mode gyroscopes, 3-D MEMS wineglass resonators, and microglassblowing of low internal loss materials.

Alexander A. Trusov (M'06) received the B.S. and M.S. degrees in applied mathematics and mechanics from Moscow State University, Moscow, Russia, in 2004, and the M.S. and Ph.D. degrees in mechanical and aerospace engineering from the University of California, Irvine (UCI), CA, USA, in 2006 and 2009, respectively. From 2009 to 2013, he was a Project Scientist with the Mechanical and Aerospace Department, UCI, where he served as the PI and a Co-PI on more than half a dozen of DoD sponsored projects. He is currently a Senior Research Scientist with Northrop Grumman Corporation, where he focuses on research and development of advanced navigation sensors and instruments. He has authored over 60 journal and conference papers, and has five issued U.S. patents (half a dozen more pending) on these topics. His research interests include design, modeling, fabrication, and vacuum packaging of micromachined inertial systems; sensor and instrument self-calibration; design of characterization experiments; and statistical data processing and analysis. He is a Member of the American Society of Mechanical Engineers and the Institute of Noetic Sciences. He was a recipient of the Outstanding Paper Award at Transducers 2011, the Design Contest Award at the System-on-Chip Conference 2011, and the best paper award at the IMAPS Device Packaging Conference 2012. He currently serves on program committees for the Saint Petersburg International Conference on Integrated Navigation Systems, the IEEE International Symposium on Inertial Sensors and Systems, and the IEEE/ION Position Location and Navigation Symposium.

Andrei M. Shkel (S'95–A'98–SM'08–F'00) received the Diploma (Hons.) degree in mechanics and mathematics from Moscow State University, Russia, in 1991, and the Ph.D. degree in mechanical engineering from the University of Wisconsin, Madison, USA, in 1997. In 2000, he joined the faculty of the University of California, Irvine, where he is currently a Professor with the Department of Mechanical and Aerospace Engineering, with a joint appointment with the Department of Electrical Engineering and Computer Science, and the Department of Biomedical Engineering.

He served as a Program Manager with the Microsystems Technology Office of the Defense Advanced Research Projects Agency (DARPA), Arlington, VA, from 2009 to 2013, where he created and managed a comprehensive portfolio of programs focused on microtechnology for positioning, navigation, and timing applications, including the programs micro rate integrating gyroscope, primary and secondary calibration on active layer, timing and inertial measurement unit, and chip-scale combinatorial atomic navigator. His professional interests, reflected in over 200 publications and two books, include solid-state sensors and actuators, microelectromechanical (MEMS)-based neuroprosthetics, sensor-based intelligence, and control theory. He holds 26 U.S. and world-wide patents. His current interests center on the design, manufacturing, and advanced control of MEMS for biomedical and inertial navigation applications, in particular, on the development of high-precision micromachined gyroscopes. He has served on a number of editorial boards, most recently as an Editor of the IEEE JOURNAL OF MICROELECTROMECHANICAL SYSTEMS and the *ASME Journal of Microelectromechanical Systems*, an Editorial Board Member of the *International Journal on Smart Structures and Systems*, the Founding Chair of the IEEE International Symposium on Inertial Sensors and Systems, and the General Chair of the 2005 IEEE Sensors Conference. He received the IEEE Sensors Council 2009 Technical Achievement Award, the 2005 NSF CAREER Award, the 2002 George E. Brown, Jr. Award, and the 2006 Best Faculty Research Award.

Dr. Shkel received the Office of the Secretary of Defense Medal for Exceptional Public Service for his work at DARPA as a Program Manager in 2013.